Available online at www.sciencedirect.com
SCIENCE DIRECT
Applied Catalysis A: General 303 (2006) 166–176
APPLIED CATALYSIS A: GENERAL
www.elsevier.com/locate/apcata

Modeling the high-temperature catalytic partial oxidation of methane over platinum gauze: Detailed gas-phase and surface chemistries coupled with 3D flow field simulations

Raúl Quiceno [a,b], Javier Pérez-Ramírez [b], Jürgen Warnatz [a], Olaf Deutschmann [c,*]

[a] *Interdisciplinary Center for Scientific Computing, University of Heidelberg, Im Neuenheimer Feld 368, D-69120 Heidelberg, Germany*
[b] *Laboratory for Heterogeneous Catalysis, Catalan Institution for Research and Advanced Studies (ICREA) and Institute of Chemical Research of Catalonia (ICIQ), Av. Paisos Catalans 16, E-43007, Tarragona, Spain*
[c] *Institute for Chemical Technology and Polymer Chemistry, University of Karlsruhe, Engesserstr. 20, D-76131 Karlsruhe, Germany*

Received 7 September 2005; received in revised form 24 January 2006; accepted 26 January 2006
Available online 24 March 2006

Abstract

The high-temperature catalytic partial oxidation (CPO) of methane over a platinum gauze reactor was modeled by three-dimensional numerical simulations of the flow field coupled with heat transport as well as detailed gas-phase and surface reaction mechanisms. Model results agree well with data of CPO experiments over Pt-gauzes in the literature, confirming the presence of strong mass and heat-transport limitations. The conversions of CH_4 and O_2 increase with an increased contact time and were practically constant in the temperature range of 1000–1200 K. The selectivity to CO linearly increases with temperature. H_2 was only observed above 1200 K, below this temperature H_2O was the only hydrogen-containing product. The contribution of heterogeneous steps in the overall process is prominent, but in the later stages of the reactor, gas-phase reactions become significant at certain conditions of temperature, pressure, and residence time. For example, simulations predicted some gas-phase production of ethane and ethylene via methane oxidative coupling at elevated pressure and residence time. The study shows that today's CFD tools allow the implementation of detailed homogeneous and heterogeneous reaction schemes even for complex catalyst geometries.

Keywords: Methane partial oxidation; Pt metal gauze; CFD; Modeling; Reaction mechanisms

1. Introduction

The application of high-temperature catalysis for the conversion of alkanes to more useful chemicals is often characterized by a complex interplay between transport processes and chemical reactions, which may also occur in the gas phase. The overall reaction rate is often mass and/or heat-transfer limited [1] and the adequate integration of physical (transport) and chemical (reaction mechanisms) processes is a key in model development and the way to a solid understanding leading to optimal reactor design and operation.

The high-temperature catalytic partial oxidation (CPO) of methane in short contact time (milliseconds) reactors [2] has been intensively studied, because it offers a promising route to convert natural gas into synthesis gas (H_2 and CO), which can subsequently be converted to higher alkanes or methanol. Catalytic reactors for methane oxidation include noble metal coated foams [2–4], monoliths [5–10], wire gauzes [11,12], or sintered spheres [13–15]. While numerical simulations of monolithic structures meanwhile applied detailed flow and chemistry models even for transient processes [9], simulations of wire gauze reactors have used either simplifying two-dimensional flow geometries or lumped reaction schemes [16–19].

A notable exception considering geometric effects are the studies by Marin and co-workers [18,19]. They studied the partial oxidation of methane performing steady-state tests in a

* Corresponding author. Tel.: +49 721 6083138; fax: +49 721 6084805.
E-mail address: deutschmann@ict.uni-karlsruhe.de (O. Deutschmann).

0926-860X/$ – see front matter © 2006 Elsevier B.V. All rights reserved.
doi:10.1016/j.apcata.2006.01.041

continuous flow-reactor containing a single platinum gauze. Due to its complexity, the gauze was simplified to a two-dimensional structure, so-called flat reactor model, in order to develop a kinetic model for CPO in the presence of heat and mass transport limitations. Then, the three-dimensional structure of the wire gauze was simulated using a simple surface reaction; gas-phase reactions had not to be considered [18].

The present simulation study of CPO of CH_4 over a Pt gauze reactor applies a three-dimensional flow field description coupled with a heat balance and detailed schemes for gas-phase and surface chemistries. This model closely describes realistic reactor features and it can be confidently extrapolated to simulate unprecedented experimental conditions. The results indicate that both homogeneous and heterogeneous processes can be simultaneously implemented in a CFD simulation in order to accomplish solid reactor modeling.

2. Reactor modeling

2.1. Gauze reactor and computational domain

The present study is based on the gauze configuration reported by de Smet et al. [18,19], as schematically shown in Fig. 1. The gauze catalyst consists of two rows of six parallel platinum wires placed on top of each other (Fig. 1a). The average distance between the centers of two individual wires (diameter = 0.20 mm) was 0.82 mm (Fig. 1b).

Due to symmetry considerations, only a quarter of the single mesh of the gauze catalyst has to be analyzed. The computational domain includes a single contact point between two wires and half the distance between the centers of two individual wires (amount 0.41 mm) in the *Y*-direction (Fig. 1c). In the CFD simulations, the total number of computational cells is 35,675 with 7571 nodes. One thousand four hundred twelve of the computational cells have boundaries with the wire surface, at which catalytic reactions occur.

At the reactor inlet, 0.5 mm upstream the gauze, the reactive mixture (volumetric CH_4/O_2 ratio = 2.5 diluted by 80 vol.% He) flows at a uniform inlet velocity of 10 m/s at 600 K. The downstream extension of the computational domain is 2.5 mm behind the gauze. The wire temperature can additionally be adjusted by resistive heating.

2.2. Numerical model

Modeling the gauze reactor involves a numerical solution of the Navier–Stokes equations, in which detailed surface and gas-phase reaction mechanisms are integrated. Gas-phase and

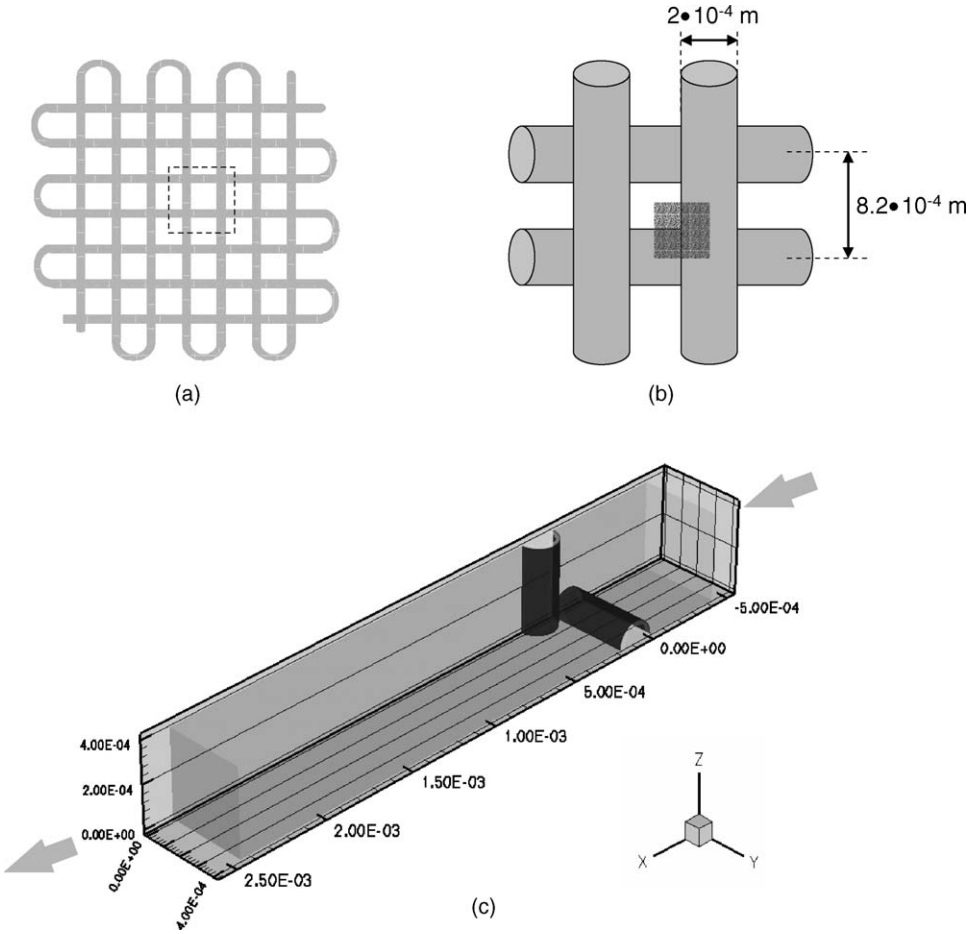

Fig. 1. Sketch of the platinum gauze: (a) original gauze and (b) detail of wire intersections, where the shadow area corresponds to the selected computational domain presented in (c).

Table 1
Gas-phase reaction mechanism

Reaction	A (mol, cm, s)	β	E_a (kJ/mol)
$O_2 + H = OH + O$	9.756×10^{13}	0.0	62.10
$H_2 + OH = H_2O + H$	1.000×10^{8}	1.600	13.80
$H + O_2 + M_3 = HO_2 + M_3$	2.100×10^{18}	−0.800	0.0
$HO_2 + H = OH + OH$	1.500×10^{14}	0.0	3.80
$HO_2 + H = H_2 + O_2$	3.000×10^{13}	0.0	4.00
$HO_2 + H = H_2O + O$	3.000×10^{13}	0.0	7.20
$HO_2 + OH = H_2O + O_2$	6.000×10^{13}	0.0	0.0
$HO_2 + HO_2 = H_2O_2 + O_2$ [a]	4.220×10^{14}	0.0	50.14
$HO_2 + HO_2 = H_2O_2 + O_2$ [a]	1.320×10^{11}	0.0	−6.82
$H_2O_2 + OH = H_2O + HO_2$	5.400×10^{12}	0.0	4.20
$OH + OH + M_1 = H_2O_2 + M_1$	7.230×10^{13}	−0.370	0.0
Low	5.530×10^{19}	−0.760	0.0
Troe	0.50, 0.0	0.0	0.0
$CO + OH = CO_2$+H	4.760×10^{7}	1.230	0.29
$CO + HO_2 = CO_2 + OH$	1.500×10^{14}	0.0	98.70
$CO + CH_3O = CO_2 + CH_3$	1.580×10^{13}	0.0	49.40
$CHO + M_1 = CO + H + M_1$	4.500×10^{14}	0.0	66.00
$CHO + O_2 = CO + HO_2$	2.400×10^{12}	0.0	0.0
$CHO + O_2 = CO_2 + OH$	0.600×10^{12}	0.0	0.0
$CHO + HO_2 = OH + CO_2 + H$	3.000×10^{13}	0.0	0.0
$CH_2O + H = CHO + H_2$	1.270×10^{8}	1.62	9.00
$CH_2O + O = CHO + OH$	4.150×10^{11}	0.57	11.60
$CH_2O + OH = CHO + H_2O$	3.400×10^{9}	1.18	−1.87
$CH_2O + HO_2 = CHO + H_2O_2$	3.000×10^{12}	0.0	54.7
$CH_2O + CH_3 = CHO + CH_4$	7.830×10^{-8}	6.1	8.20
$CH_2O + O_2 = CHO + HO_2$	6.000×10^{13}	0.0	170.70
$CH_3 + O_2 = CH_2O + OH$	3.300×10^{11}	0.0	37.40
$CH_3 + HO_2 = CH_3O + OH$	1.800×10^{13}	0.0	0.0
$CH_3 + HO_2 = CH_4 + O_2$	3.600×10^{12}	0.0	0.0
$CH_3 + CH_3 + M_1 = C_2H_6 + M_1$	3.610×10^{13}	0.0	0.0
Low	3.630×10^{41}	−7.000	11.60
Troe	0.620, 73.0	1180.0	0.0
$CH_3O + M_1 = CH_2O + H + M_1$	5.000×10^{13}	0.0	105.0
$CH_3O + O_2 = CH_2O + HO_2$	3.000×10^{10}	0.0	7.3
$CH_2O + CH_3O = CH_3OH + CHO$	1.150×10^{11}	0.0	5.2
$CH_3 + O_2 \rightarrow O + CH_3O$	0.600×10^{14}	0.0	131.0
$CH_2OH + O_2 = CH_2O + HO_2$	1.570×10^{15}	0.0	0.0
$CH_3 + O_2 + M_1 = CH_3O_2 + M_1$	7.800×10^{8}	1.2	0.0
Low	1.650×10^{26}	−3.30	0.0
Troe	0.495, 2325.5	10.0	0.0
$CH_3O_2 + CH_2O = CH_3O_2H + CHO$	2.000×10^{12}	0.0	48.74
$CH_3O_2 + CH_3 = CH_3O + CH_3O$	2.400×10^{13}	0.0	0.0
$CH_3O_2 + HO_2 = CH_3O_2H + O_2$	2.400×10^{11}	0.0	−6.6
$CH_4 + H = H_2 + CH_3$	1.330×10^{4}	3.00	33.60
$CH_4 + O = OH + CH_3$	6.923×10^{8}	1.56	35.50
$CH_4 + OH = H_2O + CH_3$	1.000×10^{7}	1.83	11.60
$CH_4 + HO_2 = H_2O_2 + CH_3$	1.100×10^{13}	0.0	103.10
$CH_4 + CH_3O = CH_3OH + CH_3$	4.300×10^{12}	0.0	42.00
$CH_4 + CH_3O_2 = CH_3O_2H + CH_3$	1.8100×10^{11}	0.0	77.80
$CH_3OH + H = CH_2OH + H_2$	1.640×10^{07}	2.0	18.89
$CH_3OH + OH = CH_2OH + H_2O$	1.440×10^{06}	2.0	−3.5
$CH_3OH + OH = CH_3O + H_2O$	1.640×10^{13}	0.0	−7.1
$CH_3OH + HO_2 = CH_2OH + H_2O_2$	9.640×10^{10}	0.0	52.58
$CH_3OH + CH_3 = CH_4 + CH_2OH$	9.000×10^{12}	0.0	41.1
$CH_3O_2H = CH_3O + OH$	6.000×10^{14}	0.0	177.10
$CH_3O_2 + H_2O_2 = CH_3O_2H + HO_2$	2.400×10^{12}	0.0	41.8
$CH_3 + CO + M_1 = CH_3CO + M_1$	5.058×10^{11}	0.0	28.77
$C_2H_4 + CH_3O = OXIRAN + CH_3$	1.000×10^{11}	0.0	60.61
$CH_3CHO + OH = CH_3CHO + H_2O$	2.300×10^{10}	0.73	−4.6
$CH_3CHO + HO_2 = CH_3CO + H_2O_2$	3.100×10^{12}	0.0	50.0
$CH_3CHO + CH_3 = CH_3CO + CH_4$	2.050×10^{-06}	5.6	10.3

Table 1 (*Continued*)

Reaction	A (mol, cm, s)	β	E_a (kJ/mol)
$CH_3CO + O = CO_2 + CH_3$	4.818×10^{23}	0.0	0.0
$C_2H_4 + H + M_1 = C_2H_5 + M_1$	2.000×10^{09}	1.28	5.4
Low	16.980×10^{18}	0.0	3.2
Troe	0.760, 40.0	1025.0	0.0
$C_2H_5 + M_1 = C_2H_4 + H + M_1$	8.200×10^{13}	0.0	166.8
Low	3.400×10^{17}	0.0	139.6
Troe	0.750, 97.0	1379.0	0.0
$C_2H_6 + H = C_2H_5 + H_2$	1.150×10^{09}	1.9	31.1
$C_2H_6 + OH = C_2H_5 + H_2O$	6.200×10^{06}	2.0	3.6
$C_2H_6 + HO_2 = C_2H_5 + H_2O_2$	1.333×10^{13}	0.0	85.6
$C_2H_6 + CH_3 = C_2H_5 + CH_4$	1.000×10^{13}	0.0	56.54
$C_2H_6 + CH_3O = CH_3OH + C_2H_5$	2.409×10^{11}	0.0	29.68
$OXIRAN + H = C_2H_3O + H_2$	8.010×10^{13}	0.0	40.50
$OXIRAN + OH = C_2H_3O + H_2O$	6.625×10^{12}	0.0	12.14
$OXIRAN + CH_3 = C_2H_3O + CH_4$	1.072×10^{12}	0.0	49.47
$OXIRAN = CH_3CHO$	6.310×10^{13}	0.0	247.71
$OXIRAN = CH_4 + CO$	1.210×10^{13}	0.0	239.46
$OXIRAN = CH_3 + CHO$	3.630×10^{13}	0.0	239.46
$C_2H_5 + M_1 + O_2 = C_2H_5O_2 + M_1$	2.002×10^{42}	−10.3	25.44
$C_2H_5O_2 \rightarrow DC_2OOH$	2.080×10^{12}	0.0	138.0
$DC_2OOH \rightarrow C_2H_5O_2$	8.500×10^{09}	−0.09	69.5
$DC_2OOH \rightarrow OXIRAN + OH$	1.300×10^{10}	0.0	65.5
$C_2H_5O_2 + HO_2 = C_2H_5OOH + O_2$	9.697×10^{10}	0.0	−10.47
$C_2H_5O_2 + CH_2O \rightarrow C_2H_5OOH + CHO$	1.000×10^{12}	0.0	42.0
$C_2H_5OOH + CHO \rightarrow C_2H_5O_2 + CH_2O$	2.700×10^{06}	1.0	0.688

With the third body efficiencies

M_1	H_2/1.0/	H_2O/6.5/	O_2/0.4/	He/0.35/	CO/0.75/	CO_2/1.5/	CH_4/3.0/
M_3	H_2/1.0/	H_2O/6.5/	O_2/0.4/	He/0.29/	CO/0.75/	CO_2/1.5/	CH_4/3.0/

The mechanism can be downloaded from http://www.detchem.com/mechanisms.

[a] The rate law of this reaction is represented by addition of both kinetic rates.

surface chemistry is coupled by adsorption and desorption of stable and radical species. For each chemical species one additional conservation equations is solved. The dependence of the transport properties such as viscosity, diffusion coefficients, and heat conduction on composition and temperature is taken into account. The heat balance considered heat convection, conduction in the gas- and solid-phase, and heat release by chemical reactions. Modified Arrhenius expressions are assumed to model the reaction rate in the chemical source terms. The thermodynamic data were obtained by polynomial fits as given in commonly used thermodynamic databases [20–22].

The flow field was computed using the commercial computational fluid dynamics code FLUENT [23], which was coupled with external subroutines (user defined functions = UDFs) to model gas-phase and surface chemistries based on the software package DETCHEM [24]. In those UDFs, in every numerical iteration and for all computational cells in the gas-phase, the reaction rate of each chemical species is calculated from an elementary-step reaction mechanism at the locally given temperature and concentrations. Furthermore, the reaction enthalpies are provided. At all computational cells with catalytically active (surface reactions) boundaries, DETCHEM provides the surface mass fluxes of each species due to adsorption and desorption as well as the reaction enthalpies at the locally given gas-phase concentrations and temperature, again at every numerical iteration. The calculation of these catalytic source terms is based on a multi-step reaction mechanism and the calculation of the local surface coverages with adsorbed species. Therefore, the surface coverages are evaluated by solving Eq. (13) for every numerical iteration. The computation of the chemical source terms is the most CPU time consuming part of the CFD simulation. The equation system is given in Appendix A.

3. Results and discussion

3.1. Reaction mechanisms

The partial oxidation of methane is catalyzed by a number of metal surfaces, although common mechanistic and kinetic features can be discerned. It is experimentally observed that increasing the temperature or lowering the feed CH_4/O_2 ratio lead to increased methane conversion. The yield of CO_x increases with temperature and oxygen concentration at the reactor inlet. Products of methane oxidative coupling (C_2 and higher hydrocarbons) have been observed at temperatures above 873 K [25], in particular at low methane conversion [26]. The first step in the catalytic partial oxidation of methane involves the cleavage of a C–H bond at the catalyst surface [25,27] leading to highly reactive CH_3 species. Heterogeneous

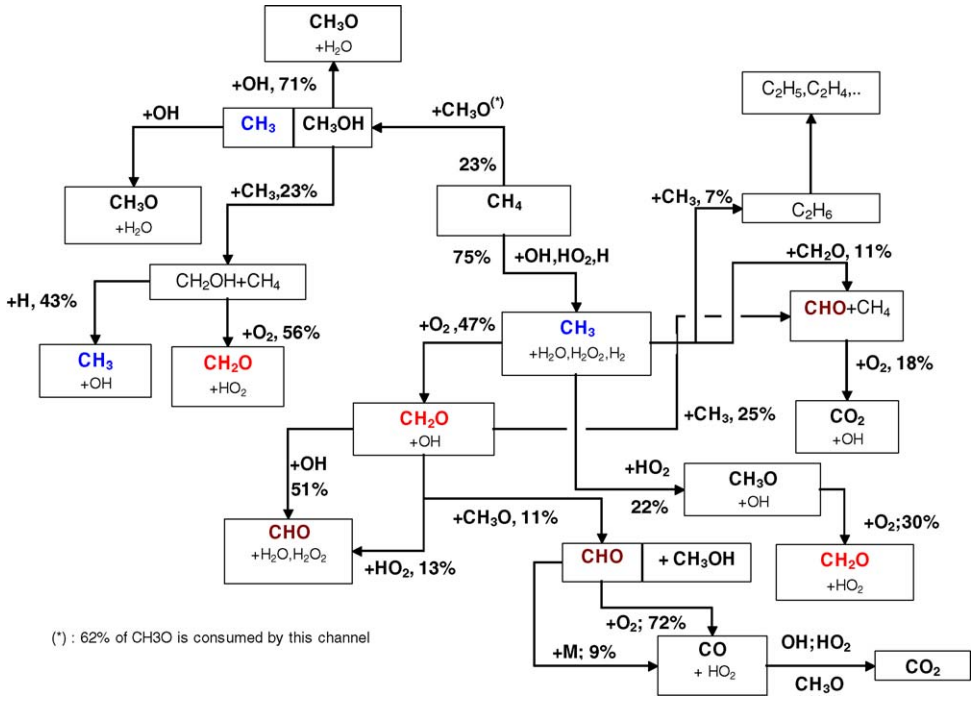

Fig. 2. Reaction path analysis of a homogeneous simulation of methane oxidation in the gas phase. Percentages in the flow analysis quantify the channel contribution to the species consumption in each step. Conditions: CH_4/O_2 vol. ratio = 2.5, constant reactor temperature = 1050 K, pressure = 1 bar. The residence time was fixed in order to achieve a methane conversion of 5%.

steps at the catalyst surface involving methyl groups and surface oxygen are mainly responsible for CO and CO_2 formation, although some authors have indicated a certain contribution of secondary gas-phase oxidation of C_2 species [28–30]. Originally, the oxidative coupling process was thought to occur only at the catalyst surface [31]. However, Ito et al. [28] postulated that the recombination of two methyl radicals leading to C_2H_6 occurs on the catalyst surface as well as in the gas phase. Lunsford and co-workers [29] identified gas-phase methyl radicals during the partial oxidation of methane, further supporting the relevance of homogeneous reactions in the oxidative coupling of methane to ethane. The above experimental evidence underlines the importance of coupling gas-phase and surface reaction mechanisms for developing robust kinetic schemes able to simulate the high-temperature catalytic partial oxidation of methane in the millisecond regime.

3.1.1. Gas-phase reaction mechanism

The gas-phase mechanism was derived from a previously proposed mechanism for the total oxidation of C_1–C_4 alkanes at high-temperature (>1200 K) [32]. In that study, the resulting micro-kinetic model was evaluated by comparing experiments and simulations related to ignition delay times, flame velocities, and concentration profiles of species as a function of time for a wide range of conditions. The existing mechanism was extended by an additional set of automatically generated elementary steps for the reactions at lower temperatures [33] and several schemes for partial oxidation and pyrolysis reactions in the temperature range of 700–1100 K [33].

The automatic generation method is based on the fact that even if detailed reaction mechanisms involve several hundred of chemical species taking part in thousands of elementary reactions, only a very limited number of different reactions types appear. The most important reactions types of the mechanism of hydrocarbons are [34,35]: decomposition of hydrocarbons, H-atom abstraction by small reactive species, β-scission of radicals, internal H-atom abstraction, addition of molecular oxygen and O–O bond scission. The rate coefficients of these reactions depend on the radical abstracting an H-atom, the type of H-atom being abstracted (primary, secondary or tertiary), the number of available equivalent H-atoms and the size of the structure. It is possible to formulate these reactions and their rate expressions using reactions rules, starting from an initial mixture of species and the elementary reactions rules.

The second extension of the mechanism is based on experimental studies of oxidation and reforming of single-component fuels (methane, ethane, propane, and butane) as well as their mixtures. The proposed mechanism accurately describes the ignition delay times and the product composition as function of temperature and residence time [35].

This total gas-phase mechanism consists of 1428 irreversible reactions among 146 species. The semi-empirical Troe formalism [36] is applied to describe the kinetics of pressure-dependent reactions. For the current study, the mechanism was simplified in order to speed up the CFD simulation. Sensitivity and flow analysis was carried out for homogeneous conditions to find and remove reaction paths, which are insignificant for CPO of methane at the conditions chosen. The temperature, pressure, and contact times used for this analysis were chosen accordingly to the 3D gauze reactor experiment. Simulations performed for the homogeneous process alone revealed that isolated gas-phase reactions were

Table 2
Surface reaction mechanism

Reaction	A (cm, mol, s)	β	E_a (kJ/mol)	μ_{ik}	ε_{ik}	[a]
$H_2 + Pt_{(S)} + Pt_{(S)} \rightarrow H_{(S)} + H_{(S)}$	0.0460[b]	0.0	0.0	−1.0	0.0	$Pt_{(S)}$
$O_2 + Pt_{(S)} + Pt_{(S)} \rightarrow O_{(S)} + O_{(S)}$	1.890×10^{21}	−0.5	0.0			
$CH_4 + Pt_{(S)} + Pt_{(S)} \rightarrow CH_{3(S)} + H_{(S)}$	0.0009[b]	0.0	72.0			
$CH_4 + O_{(S)} + Pt_{(S)} \rightarrow CH_{3(S)} + OH_{(S)}$	5.000×10^{18}	0.7	42.0	0.0	−8.0	$O_{(S)}$
$CH_4 + OH_{(S)} + Pt_{(S)} \rightarrow CH_{3(S)} + H_2O_{(S)}$	1.0000[b]	0.0	10.0			
$H_2O + Pt_{(S)} \rightarrow H_2O_{(S)}$	0.7500[b]	0.0	0.0			
$CO_2 + Pt_{(S)} \rightarrow CO_{2(S)}$	0.0050[b]	0.0	0.0			
$CO + Pt_{(S)} \rightarrow CO_{(S)}$	0.8400[b]	0.0	0.0			
$H_{(S)} + H_{(S)} \rightarrow Pt_{(S)} + Pt_{(S)} + H_2$	3.700×10^{21}	0.0	67.4	0.0	10.0	$H_{(S)}$
$O_{(S)} + O_{(S)} \rightarrow Pt_{(S)} + Pt_{(S)} + O_2$	3.700×10^{21}	0.0	235.5	0.0	188.3	$O_{(S)}$
$H_2O_{(S)} \rightarrow H_2O + Pt_{(S)}$	4.500×10^{12}	0.0	41.8			
$CO_{(S)} \rightarrow CO + Pt_{(S)}$	1.000×10^{15}	0.0	146.0	0.0	33.0	$CO_{(S)}$
$CO_{2(S)} \rightarrow CO_2 + Pt_{(S)}$	1.000×10^{13}	0.0	27.1			
$C_{(S)} + O_{(S)} \rightarrow CO_{(S)} + Pt_{(S)}$	3.700×10^{19}	0.0	0.0			
$CO_{(S)} + Pt_{(S)} \rightarrow C_{(S)} + O_{(S)}$	3.700×10^{19}	0.0	236.5	0.0	33.0	$CO_{(S)}$
$CO_{(S)} + O_{(S)} \rightarrow CO_{2(S)} + Pt_{(S)}$	3.700×10^{19}	0.0	117.6	0.0	33.0	$CO_{(S)}$
$CO_{2(S)} + Pt_{(S)} \rightarrow CO_{(S)} + O_{(S)}$	3.700×10^{19}	0.0	173.3	0.0	−94.1	$O_{(S)}$
$CO_{(S)} + OH_{(S)} \rightarrow CO_{2(S)} + H_{(S)}$	1.000×10^{19}	0.0	38.7	0.0	30.0	$CO_{(S)}$
$CO_{2(S)} + H_{(S)} \rightarrow CO_{(S)} + OH_{(S)}$	1.000×10^{19}	0.0	8.4			
$CH_{3(S)} + Pt_{(S)} \rightarrow CH_{2(S)} + H_{(S)}$	1.260×10^{22}	0.0	70.3			
$CH_{2(S)} + H_{(S)} \rightarrow CH_{3(S)} + Pt_{(S)}$	3.090×10^{22}	0.0	0.0	0.0	2.8	$H_{(S)}$
$CH_{2(S)} + Pt_{(S)} \rightarrow CH_{(S)} + H_{(S)}$	7.310×10^{22}	0.0	58.9	0.0	−50.0	$C_{(S)}$
$CH_{(S)} + H_{(S)} \rightarrow CH_{2(S)} + Pt_{(S)}$	3.090×10^{22}	0.0	0.0	0.0	2.8	$H_{(S)}$
$CH_{(S)} + Pt_{(S)} \rightarrow C_{(S)} + H_{(S)}$	3.090×10^{22}	0.0	0.0	0.0	2.8	$H_{(S)}$
$C_{(S)} + H_{(S)} \rightarrow CH_{(S)} + Pt_{(S)}$	1.250×10^{22}	0.0	138.0			
$H_{(S)} + O_{(S)} \rightarrow OH_{(S)} + Pt_{(S)}$	1.280×10^{21}	0.0	11.2			
$OH_{(S)} + Pt_{(S)} \rightarrow H_{(S)} + O_{(S)}$	7.390×10^{19}	0.0	77.3	0.0	73.2	$O_{(S)}$
$H_2O_{(S)} + Pt_{(S)} \rightarrow H_{(S)} + OH_{(S)}$	1.150×10^{19}	0.0	101.4	0.0	−167.3	$O_{(S)}$
$OH_{(S)} + OH_{(S)} \rightarrow H_2O_{(S)} + O_{(S)}$	7.400×10^{20}	0.0	74.0			
$H_2O_{(S)} + O_{(S)} \rightarrow OH_{(S)} + OH_{(S)}$	1.000×10^{20}	0.0	43.1	0.0	−240.6	$O_{(S)}$
$H_2 + C_{(S)} \rightarrow CH_{2(S)}$	0.0400[b]	0.0	29.7	0.0	−4.6	$C_{(S)}$
$CH_{2(S)} \rightarrow C_{(S)} + H_2$	7.690×10^{13}	0.0	25.1	0.0	−50.0	$C_{(S)}$
$H_{(S)} + OH_{(S)} \rightarrow H_2O_{(S)} + Pt_{(S)}$	2.040×10^{21}	0.0	66.22			
$CH_{3(S)} + H_{(S)} \rightarrow CH_4 + Pt_{(S)} + Pt_{(S)}$	3.300×10^{21}	0.0	50.0	0.0	2.8	$H_{(S)}$
$CH_{3(S)} + H_2O_{(S)} \rightarrow CH_4 + OH_{(S)} + Pt_{(S)}$	3.700×10^{21}	0.0	110.6			
$CH_{3(S)} + OH_{(S)} \rightarrow CH_4 + O_{(S)} + Pt_{(S)}$	3.700×10^{21}	0.0	87.9			

The surface site density, Γ, is 2.72×10^{-5} mol/m^2. The mechanism can be downloaded from http://www.detchem.com/mechanisms.
[a] Denotes the species i, to which the parameter μ_{ik} and ε_{ik} refer to, see Eq. (12).
[b] Sticking coefficient.

not significant. This is related to the fact that the homogeneous processes are initiated by radicals, which may also desorb from the platinum surface. The resulting mechanism consists of 150 irreversible reactions among 30 species. Table 1 summarizes all reaction steps and the associated kinetic data.[1] The major reaction pathways for CPO of methane are schematically shown in Fig. 2 for a volumetric CH_4/O_2 ratio of 2.5 at 1050 K and atmospheric pressure. The residence time of 36 s corresponds to a methane conversion of 5%. This analysis reveals that the reaction network becomes rather complex even for the simple fuels such as methane.

3.1.2. Surface reaction mechanism

The surface reaction mechanism used in the simulation is based on a mechanism developed for the prediction of ignition and steady-state operation of catalytic combustion of methane over platinum [27]. The original scheme, which includes 10 surface species, 9 reversible reactions, and 8 irreversible reactions, takes into account interactions between the gas-phase and surface mechanisms via molecular (CH_4, O_2, CO, CO_2, H_2O, and H_2) and radical (H, O, and OH) species. In the present work, this mechanism is extended by additional elementary steps proposed in a study on oxidative dehydrogenation of ethane over platinum coated monolithic structures [37]. Their mechanism consists of 19 surface species and 41 reversible reactions steps, and includes the complete C_1 surface mechanism with initial adsorption steps for methane with surface atomic oxygen and hydroxyl species. These pathways are included in the original mechanism, finally resulting in the set of elementary steps shown in Table 2. The additional C_2 species of this ethane mechanism [37] are not included in the present work, because there are not expected to have any influence on the conversion.

[1] Both the full and the reduced mechanism can be downloaded from http://www.detchem.com/mechanisms.

3.2. Model predictions and comparison with experimental results

The model was evaluated by comparison with the experimental results reported by de Smet et al. [18,19]. In their study, CO, CO_2, and H_2O were reported as the main reaction products at temperatures below 1270 K. Above this temperature, H_2 formation was additionally observed. Fig. 3 compares the experimental results from this study with our computed values at a CH_4/O_2 ratio of 2.5, an axial flow velocity of 10 m/s, inlet temperature of 600 K, and a pressure of 1.3 bar. CH_4 and O_2 conversion are not temperature dependent, while the CO selectivity is strongly influenced by the temperature. The simulation predicts the experimental data quite well. The computed conversion of oxygen is slightly higher than the experimental values. The data are also in agreement with those from Heitnes et al. [38] and Hickman and Schmidt [39] over Pt and Pt–Rh alloy gauzes.

Fig. 4a–f presents typical profiles of temperature, velocity, and species mole fractions (CH_4, O_2, CO_2, CO, and H_2O)

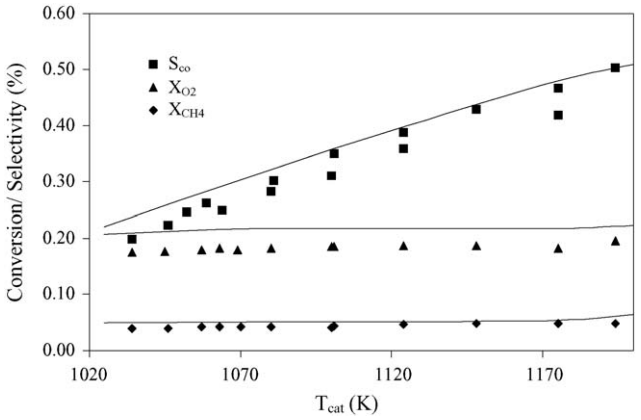

Fig. 3. Comparison of experimental data (symbols) and predicted methane and oxygen conversion (X) and CO selectivity (S) as function of catalyst temperature. Conditions: CH_4/O_2 vol. ratio = 2.5, axial inlet flow velocity = 10 m/s, inlet temperature = 600 K, and pressure = 1.3 bar.

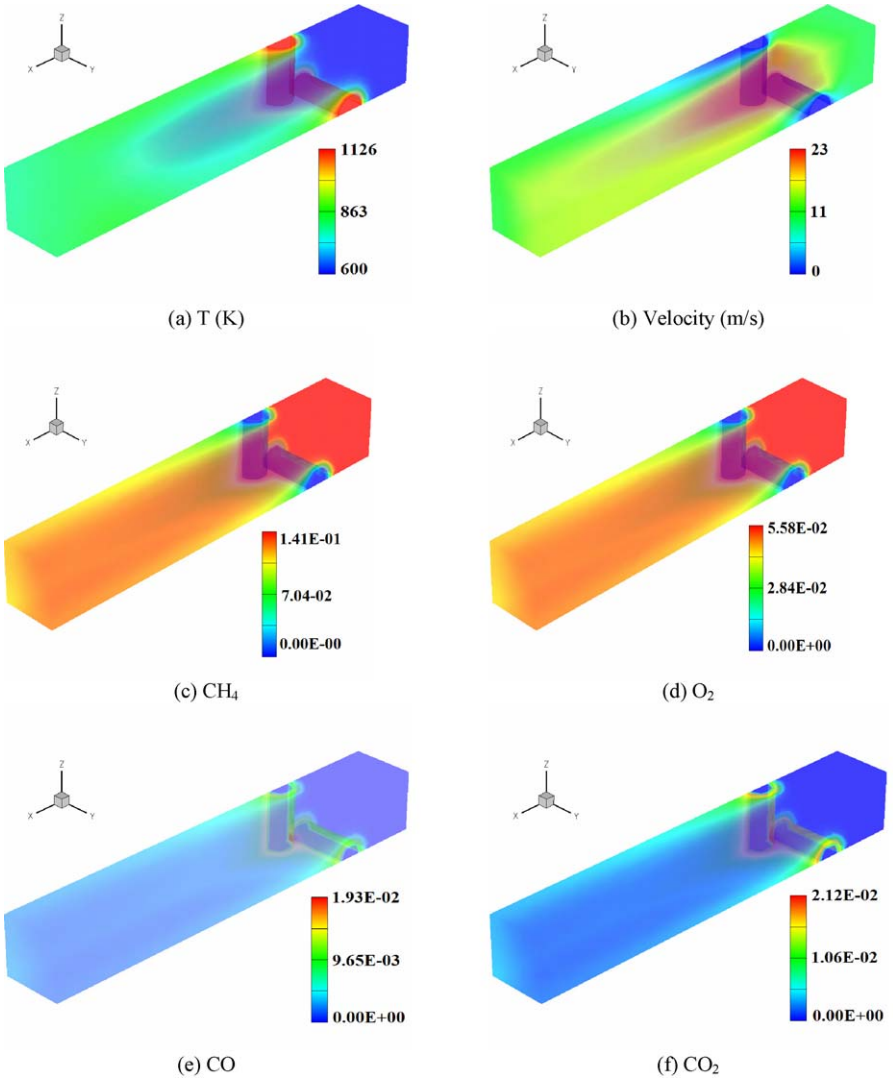

Fig. 4. Numerically predicted contour profiles of temperature, magnitude of velocity, and mole fractions of the major species. Conditions: CH_4/O_2 vol. ratio = 2.5, axial inlet flow velocity = 10 m/s, inlet temperature = 600 K, and pressure = 1.3 bar.

resulting from the simulation over the computational domain (Fig. 1c) at a volumetric CH_4/O_2 ratio of 2.5 (80 vol.% He dilution) flows, a uniform inlet velocity of 10 m/s at 600 K and autothermal conditions. From the temperature profile (Fig. 4a) two different zones can be distinguished. First, on the top of the mesh (center of the gauze in the real reactor) the temperature is in the range of 600–800 K, which is less than 200 K above the inlet gas temperature, and the maximum value of temperature is located at the crossing point of the wires. A thin layer characterizes the second zone, which is at the bottom of the mesh next to the wires. At this point, the gas-phase temperature is similar to the wire temperature. This zone is extended to nearly half of the wire diameter downstream until it is cooled down to 800 K. The velocity profiles (Fig. 4b) show an opposite behavior than the temperature profiles: the maximum velocity occurs at the top of the mesh in the free path zone of the wire, approaching zero close to the wire surfaces.

The consumption rates of both CH_4 and O_2 reach their maximum at the surface of the platinum wires. It is worth noting that a part of the domain downstream and next to the wires experienced notable gradients of methane concentration (Fig. 4c). In this part of the domain, the velocity is nearly zero, which means that convection does not play any important role in the mass-transfer process. This vanishing velocity, however, means longer residence time of the mixture, and consequently a higher conversion is observed. The mole fraction profile of oxygen (Fig. 4d) is similar to that of methane. Both reactants are mainly consumed as the result of surface reactions, in agreement with the literature [2,25,39]. Carbon monoxide and carbon dioxide (Fig. 4e and f) are produced on the surface of the catalytic wires, with their maximal yield occurring at the crossing of the wires. Water (not shown) is produced on the surface as the only H-containing product. Hydrogen or products resulting from the oxidative coupling of methane were not observed at atmospheric pressure. Under the conditions used in these experiments, homogeneous reactions were not relevant. Simulations performed with and without the gas-phase chemistry yielded identical results for the main products, since the concentration of radical species in the gas-phase was negligible.

3.3. Influence of residence time and pressure

The influence of the gas-phase chemistry in the overall process becomes significant with increasing pressure and residence time [25]. Under these conditions, the formation of oxidative coupling products, e.g. C_2H_6, and total combustion products, i.e. CO_2 and H_2O, are expected to occur in the homogeneous phase as well, which was observed by simulation of the purely homogeneous partial oxidation of methane. The influence of the residence time on the homogeneous reactions was studied by decreasing the inlet gas velocity from 10 to 1 m/s.

Fig. 5a–d illustrates the mole fraction profiles of gas-phase radical species (HO_2, OH, and CH_3) and coupling product (C_2H_6) for an inlet flow velocity of 10 m/s at 1.3 bar and 600 K for a CH_4/O_2 volumetric ratio of 2.5. In all cases, these species

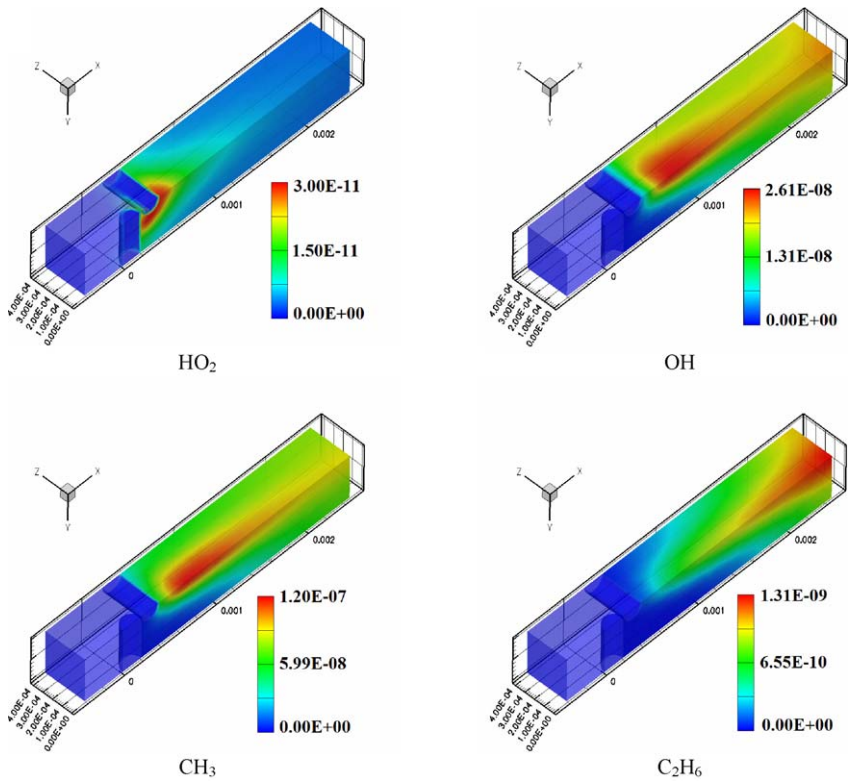

Fig. 5. Numerically predicted contour profiles of mole fractions of radical species (HO_2, HO, and CH_3) and stable products (C_2H_6). Conditions: CH_4/O_2 vol. ratio = 2.5, axial inlet flow velocity = 10 m/s, inlet temperature = 600 K, and pressure = 1.3 bar. For visual clarity the orientation of the flow direction is opposite from the one in Figs. 1 and 4.

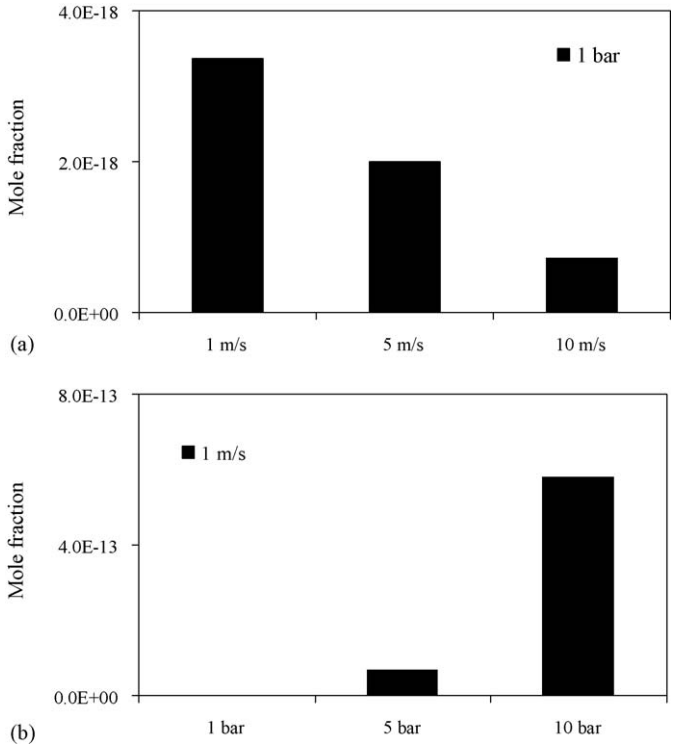

Fig. 6. Impact of (a) inlet gas velocity at 1 bar and (b) total pressure at 1 m/s on the outlet concentration of C_2H_6. Conditions: CH_4/O_2 vol. ratio = 2.5, inlet temperature = 600 K.

are formed homogeneously downstream of the gauze. The maximum production rate occurs behind the wire gauze and not behind the open area of the gauze. The domain of maximum production rate of homogeneous reactions coincides with the zone of the reactor with lower velocity and higher temperature. For the conditions considered, HO_2 is the first radical species formed, followed by hydroxyl radicals (OH) appearing at a short distance downstream. Afterwards, methyl radicals are obtained recombining and forming ethane further downstream. This result draws parallels with the reaction scheme proposed by Pollard [40] for the gas-phase oxidation of hydrocarbons in the intermediate temperature regime. Decreasing the inlet velocity from 10 to 1 m/s at fixed temperature, pressure and composition leads to an increase in conversion (4–7% for CH_4 and 20–30% for O_2), as well as a higher CO_2/CO ratio at the reactor outlet (1.0–2.0). In spite of the relevance of gas-phase processes at an increased residence time, surface chemistry is still the main route for methane conversion. It should be noted that the surface reaction mechanism does not include the adsorption/desorption of all possible radicals formed in the gas phase due to the missing knowledge of the kinetic data, which surely affects the discussion above.

Fig. 6 shows the predicted mole fraction of ethane at different pressures and inlet gas velocities. The C_2H_6 production decreases as the velocity increases (Fig. 6a), i.e. shorter residence times. An increase in pressure favors ethane production (Fig. 6b). Five orders of magnitude higher C_2H_6 yields were obtained upon increasing the pressure from 1 to 10 bar. Altogether, the total amounts of coupling products are still very low.

4. Conclusions

For the first time, the high-temperature catalytic oxidation of methane over platinum gauze has been successfully modeled using 3D numerical simulations of the flow field coupled with heat transport, and detailed gas-phase and surface kinetics based on elementary steps and surface coverage calculations. Model results are in perfect agreement with CPO experiments over Pt-gauzes reported in the literature. The simulations successfully linked the interaction between the gas-phase and the surface mechanisms through stable and radical species and the flow and diffusion around the wire catalyst. For typical conditions for CPO of methane, the heterogeneous reactions govern the overall reactor performance. However, gas-phase reactions (e.g. producing ethane via oxidative coupling) may become significant at residence times and pressures, which are longer and higher, respectively, than the one used in the present study. Accordingly, surface and gas-phase processes should be simultaneously solved with the models of the flow fields and heat transfer for a reliable description of gauze reactors.

This approach is a starting point for 3D CFD simulations with detailed heterogeneous and homogeneous reaction schemes, in particular for CPO of higher alkanes, for which both surface and gas-phase reactions are important for overall conversion, even at atmospheric pressure [37]. Former studies, for instance of CPO of hexane over wire gauzes [16], which used two-dimensional approximations of the flow field for gauze reactors can now be extended to much more realistic three-dimensional CFD simulations. The rigorous model presented can support design and optimization of gauze reactors operated at high temperature.

Acknowledgment

Funding of this study by the Deutsche Forschungsgemeinschaft (DFG) is gratefully acknowledged.

Appendix A

A.1. Numerical model

The numerical simulation is based on the Navier–Stokes equations. The basic equations without including gravitational and external body forces, thermal diffusion, and viscous heating can be written as:

$$\text{Continuity equation}: \quad \frac{\partial \rho}{\partial t} + \frac{\partial(\rho u_i)}{\partial x_i} = 0 \tag{1}$$

where ρ is the density, u_i is the cartesian components of the velocity vector, t is the time, and x_i is the cartesian coordinates.

Momentum conservation equation:

$$\frac{\partial(\rho u_i)}{\partial t} + \frac{\partial}{\partial x_j}(\rho u_i u_j) = -\frac{\partial p}{\partial x_i} + \frac{\partial \tau_{ij}}{\partial x_j} \tag{2}$$

where p is the pressure and τ_{ij} is the stress tensor, with:

$$\tau_{ij} = \left[\mu\left(\frac{\partial u_i}{\partial x_j} + \frac{\partial u_j}{\partial x_i}\right)\right] - \frac{2}{3}\mu\frac{u_1}{x_1}\delta_{ij} \tag{3}$$

where μ is the mixture viscosity and δ_{ij} is the kronecker symbol.

Species conservation equation:

$$\frac{\partial(\rho Y_i)}{\partial t} + \frac{\partial(\rho u_j Y_i)}{\partial x_j} = -\frac{\partial}{\partial x_j} j_{i,j} + R_i, \qquad i = 1, \ldots, N_g \tag{4}$$

where Y_i is the mass fraction of the specie i in the mixture, R_i is the net rate of production of species due to chemical reactions, and $j_{i,j}$ is the mass flux of the specie i in the direction j calculated as:

$$j_{i,j} = -\rho D_{i,\mathrm{m}} \frac{\partial Y_i}{\partial x_j} \tag{5}$$

where $D_{i,\mathrm{m}}$ is the diffusion coefficient of the specie i in the mixture.

Enthalpy equation:

$$\frac{\partial(\rho h)}{\partial t} + \frac{\partial(\rho u_j h)}{\partial x_j} = \frac{\partial}{\partial x_j}\left(\lambda\frac{\partial T}{\partial x_j}\right) - \frac{\partial}{\partial x_j}\sum_i^{N_g} h_i j_{i,j} + \frac{\partial p}{\partial t} + u_j\frac{\partial p}{\partial x_j} + \sum_i^{N_g} h_i R_i \tag{6}$$

where h is the enthalpy of the mixture and h_i is the enthalpy of each specie i.

The density ρ is computed using the ideal gas law. Viscosity, thermal conductivity, and the diffusion coefficient of the species in the mixture depend on the local composition and on the temperature, and are calculated via kinetic theory [41].

The enthalpy is defined as:

$$h = \sum_i^{N_g} Y_i h_i; \qquad h_i = \int_{T_{\mathrm{ref}}}^{T} c_{p,i}\,\mathrm{d}T \tag{7}$$

The conservation equations were solved using a control volume-based finite difference method. A non-staggered system was applied for storage of discrete velocities and pressure. The resulting equations were solved using SIMPLE [42] algorithm. Details about the source terms in Eqs. (4) and (6) are given below.

A.2. Gas-phase chemistry

Source terms R_i in the species and enthalpy conservation equations (R_i, $h_i R_i$), were expressed as the mass rate of creation or depletion of species i by chemical reactions. The chemical source terms are given as:

$$R_i = M_i \sum_{k=1}^{K_g} \upsilon_{ik} k_{\mathrm{f}k} \prod_{j=1}^{N_g} \left[X_j\right]^{\upsilon'_{jk}}, \qquad i = 1, \ldots, N_g \tag{8}$$

where M_i is the molar mass of the species i, K_g is the number of elementary gas-phase reactions, υ_{ik} (right side minus left side of the reaction equation) and υ'_{jk} are stoichiometric coefficients, $k_{\mathrm{f}k}$ is the forward rate coefficients, and $[X_j]$ is the concentration of species j.

The temperature dependence of the rate coefficients is described by a modified Arrhenius expression:

$$k_{\mathrm{f}k} = A_k T^{\beta_k} \exp\left[-\frac{E_{\mathrm{a}k}}{RT}\right] \tag{9}$$

where A_k is the pre-exponential factor, β_k is the temperature coefficient, $E_{\mathrm{a}k}$ is the activation energy, and R is the universal gas constant.

A.3. Surface chemistry

Chemical reactions on the solid surfaces lead to the following boundary conditions for the species governing equations:

$$j_i = F_{\mathrm{catgeo}} \dot{s}_i M_i, \qquad i = 1, \ldots, N_g \tag{10}$$

where $\vec{j}_i$ is the normal component of the diffusive flux of species i at the surface and $\dot{s}_i$ is the molar production rate of species i by adsorption and desorption. F_{catgeo} is the ratio of active catalytic surface area to geometrical surface area, which was assumed to be unity for the wire catalyst used in the present study.

The molar production rates of gas-phase and surface species are given by:

$$\dot{s}_i = \sum_{k=1}^{K_s} \upsilon_{ik} k_{\mathrm{f}k} \prod_{j=1}^{N_g+N_s} \left[X_i\right]^{\upsilon'_{jk}}, \qquad i = 1, \ldots, N_g + N_s \tag{11}$$

where K_s is the number of elementary surface reactions (including adsorption and desorption), υ_{ik} (right side minus left side of the reaction equation) and υ'_{jk} are stoichiometric coefficients, and N_s is the total number of species adsorbed. The temperature dependence of the rate coefficients is described by a modified Arrhenius expression:

$$k_{\mathrm{f}k} = A_k T^{\beta_k} \exp\left[-\frac{E_{\mathrm{a}k}}{RT}\right] \prod_{i=1}^{N_s} \Theta_i^{\mu_{ik}} \exp\left[\frac{\varepsilon_{ik}\Theta_i}{RT}\right] \tag{12}$$

This expression takes into account an additional coverage dependence using the parameter μ_{ik} and ε_{ik}, which are specified for several surface reactions. At steady-state, the time variation of the surface coverage (Θ_i) of species i is zero:

$$\frac{\partial\Theta_i}{\partial t} = \frac{\dot{s}_i}{\Gamma} = 0, \qquad i = N_g + 1, \ldots, N_g + N_s \tag{13}$$

This equation system is solved to obtain surface coverage and surface mass fluxes. The concentration $[X_i]$ of an adsorbed species is given in mol/m^2 and equals to surface coverage (Θ_i) multiplied by the surface site density (Γ).

References

[1] F. Kapteijn, J.A. Moulijn, in: G. Ertl, H. Knözinger, J. Weitkamp (Eds.), Handbook of Heterogeneous Catalysis, vol. 3, Wiley-VCH, Weinheim, Germany, 1997, p. 1189.
[2] D.A. Hickman, L.D. Schmidt, AIChE J. 39 (1993) 1164.
[3] I. Cerri, G. Saracco, V. Specchia, Catal. Today 60 (2000) 21.
[4] P. Ciambelli, V. Palma, P. Russo, S. Vaccaro, Catal. Today 75 (2002) 471.
[5] R.L. Muncrief, P. Khanna, K. Kabin, M.P. Harold, Catal. Today 98 (2004) 393.
[6] R.L. Muncrief, K. Kabin, M.P. Harold, AIChE J. 50 (2004) 2526.
[7] A. Kenji, L. Xiaohong, F. Kaoru, K. Yusaku, S. Akinori, K. Noritsugu, Y. Yoshiro, Catal. Today 84 (2003) 27.
[8] J. Krummenacher, K. West, L.D. Schmidt, J. Catal. 215 (2003) 332.
[9] R. Schwiedernoch, S. Tischer, C. Correa, O. Deutschmann, Chem. Eng. Sci. 58 (2003) 633.
[10] R. Schwiedernoch, S. Tischer, H.-R. Volpp, O. Deutschmann, Natural Gas Conversion VI, Stud. Surf. Sci. Catal. 147 (2004) 511.
[11] D.A. Goetsch, P. Witt, L.D. Schmidt, Prepr. Am. Chem. Soc., Div. Petrol. Chem. 41 (1996) 150.
[12] R.P. O'Connor, L.D. Schmidt, Stud. Surf. Sci. Catal. 133 (2001) 289.
[13] T. Nagaguchi, K. Shoji, S. Yoshida, Appl. Catal. A 133 (1995) 241.
[14] A. Jess, K. Hedden, Erdoel Erdgas Kohle 110 (1994) 365.
[15] A.S. Noskov, I.A. Zolotarskii, S.A. Pokrovskaya, V.N. Korotkikh, E.M. Slavinskaya, V.V. Mokrinskii, V.N. Kashkin, Chem. Eng. J. 91 (2003) 235.
[16] R.P. O'Connor, L.D. Schmidt, O. Deutschmann, AIChE J. 48 (2002) 1241.
[17] C.R.H. de Smet, M.H.J.M. de Croon, R.J. Berger, G.B. Marin, J.C. Schouten, AIChE J. 46 (2000) 1837.
[18] C.R.H. de Smet, M.H.J.M. de Croon, R.J. Berger, G.B. Marin, J.C. Schouten, Appl. Catal. A 187 (1999) 33.
[19] M.F. Reyniers, C.R.H. de Smet, P.G. Menon, G.B. Marin, CATTECH 6 (2002) 140.
[20] M.W. Chase, C.A. Davis, J.R. Downey, D.J. Frurip, R.A. McDonald, A.N. Syverud, J. Phys. Chem. Ref. Data 14 (1985) 927.
[21] R.J. Kee, F.M. Rupley, J.A. Miller, The Chemkin Thermodynamic Database, Sandia National Laboratories Report, SAND87-8215, 1987.
[22] A. Burcat, in: W.C. Gardiner (Ed.), Combustion Chemistry, Springer, New York, 1984.
[23] Fluent 6.0, Copyright Fluent Incorporated, Lebanon, NH, 2000, see also http://www.fluent.com.
[24] O. Deutschmann, S. Tischer, C. Correa, D. Chatterjee, S. Kleditzsch, V.M. Janardhanan, DETCHEM Software Package, 2.0 ed., Karlsruhe, 2004. see also http://www.detchem.com.
[25] J.C. Mackie, Catal. Rev. Sci. Eng. 33 (1991) 169.
[26] J.A. Sofranko, J.J. Leonard, C.A. Jones, J. Catal. 103 (1987) 302.
[27] O. Deutschmann, R. Schmidt, F. Behrendt, J. Warnatz, Proc. Combust. Inst. 26 (1996) 1747, see also http://www.detchem.com/mechanisms.
[28] T. Ito, J.X. Wang, C.H. Lin, J.H. Lunsford, J. Am. Chem. Soc. 107 (1985) 5062.
[29] K.D. Campbell, E. Morales, J.H. Lunsford, J. Am. Chem. Soc. 109 (1987) 7900.
[30] C.H. Lin, T. Ito, J.X. Wang, J.H. Lunsford, J. Am. Chem. Soc. 109 (1987) 4808.
[31] G.E. Keller, M.M. Bhasin, J. Catal. 73 (1983) 9.
[32] V. Karbach, Validierung eines detaillierten Reaktionsmechanismus zur Oxidation von Kohlenwasserstoffen bei hohen Temperaturen, Diploma Thesis, Fakultät für Chemie, Ruprecht-Karls-Universität Heidelberg, 1997.
[33] M. Nehse, Automatische Erstellung von detaillierten Reaktionsmechanismen zur Modellierung der Selbstzündung und laminarer Vormischflammen von gasförmigen Kohlenwasserstoff-Mischungen. Naturwissenschaftlich—Mathematische Gesamtfakultät, Ruprecht-Karls-Universität Heidelberg, 1999.
[34] C. Chevalier, J.W. Pitz, J. Warnatz, C.K. Westbrook, H. Melenk, Proc. Combust. Inst. 24 (1992) 93.
[35] R. Quiceno, O. Deutschmann, J. Warnatz, European Combustion Meeting 2005. Louvain-la-Neuve, 3–6 April 2005. Belgian Section of the Combustion Institute paper, Chemical Kinetics Section, paper 29.
[36] J. Troe, J. Chem. Phys. 66 (1977) 4745.
[37] D.K. Zerkle, M.D. Allendorf, M. Wolf, O. Deutschmann, J. Catal. 196 (2000) 18.
[38] K. Heitnes, S. Lindeberg, O.A. Rokstad, A. Holmen, Catal. Today 24 (1995) 211.
[39] D.A. Hickman, L.D. Schmidt, J. Catal. 138 (1992) 267.
[40] R.T. Pollard, in: C.H. Bamford, C.F.H. Tipper (Eds.), Comprehensive Chemical Kinetics Gas Phase Combustion, vol. 17, Elsevier, New York, 1977, p. 249.
[41] R.B. Bird, W.E. Stewart, E.N. Lightfoot, Transport Phenomena, John Wiley & Sons Inc., New York, 1960.
[42] S.V. Patankar, Numerical Heat Transfer and Fluid Flow, McGraw-Hill, New York, 1980.